NON-INVASIVE MICROWAVE RADIOMETRIC SYSTEM FOR INTRACRANIAL APPLICATIONS: A STUDY USING THE CONFORMAL L-NOTCH MICROSTRIP PATCH ANTENNA

N. P. Asimakis, I. S. Karanasiou *, and N. K. Uzunoglu

Microwave and Fiber Optics Laboratory
School of Electrical and Computer Engineering
National Technical University of Athens
9, Iroon Polytechneiou Street, Zografou Campus, Athens 15780, Greece

Abstract—Temperature variations in tissues inside the body have been measured using microwave radiometry for more than three decades in a variety of passive body monitoring applications. In this paper, we study a prototype system for passive intracranial monitoring using microwave radiometry. It comprises L-notch microstrip patch antennas in conjunction with a sensitive multiband microwave receiver for detection. The particular design characteristics of the antenna are its conformality and a special L cut on its upper left edge, features that make it suitable for human biomedical applications and lead to its multiband operation in the frequency range of 2–3 GHz. The theoretical electromagnetic study indicates that the radiometric contact system in question operates well at two frequencies, with satisfying detection depths and adequate portability (small dimensions). In order to verify the findings of these simulations, experimental measurements with phantoms and various setups were carried out, resulting in the definition of the actual temperature detection level and the spatial resolution of the system. Theoretical and experimental results conclude that with the appropriate combination of conformal patch antennas and microwave receiver it is possible to monitor areas of interest inside human head models with a variety of temperature resolutions and detection depths.

1. INTRODUCTION

Microwaves have been used over the years in various applications in order to support clinical practice [1–6]. Microwave radiometry was proposed approximately 30 years ago to be used as a diagnostic imaging method to noninvasively measure temperature distributions inside the human body. Since then numerous research results have been reported regarding the clinical practical value of this passive imaging methodology which exhibits unique capabilities [7, 8]. The applications of microwave radiometry in clinical medicine aim mainly at obtaining information about internal in-depth body temperature patterns by the non-traumatic measurement of natural thermal radiation from body tissues at low microwave frequencies. Knowledge of such internal body thermal patterns can assist clinical disease detection and diagnosis, e.g., as a noninvasive complement to the current computed tomography (CT) and magnetic resonance imaging (MRI) technologies [9], and may have a role in the monitoring of therapeutic processes [10], e.g., during hyperthermia [11].

Microwave radiometry allows significant penetration depth in tissues and due to its entirely passive character, an appealing application of it could realize intracranial temperature and/or conductivity variation monitoring of the human brain [12]. Noninvasive temperature monitoring may be also performed with Magnetic Resonance Spectroscopy (MRS) which can also measure temperature noninvasively (e.g., [13]) It is a well-established though not passive technique that uses an MRI scanner to detect certain naturally occurring brain metabolites with temperature precision of approximately +0.5°C [14].

Knowledge of such thermal patterns inside the brain may provide useful information about brain activity. Under normal, quiet, resting conditions intrabrain heat production is balanced by heat dissipation from the brain, while under several physiological conditions this temperature balance becomes shifted and brain temperatures either increase above (hyperthermia) or decrease below (hypothermia) their "normal" values [15, 16]). Brain hyperthermia and hypothermia may also occur following pharmacological challenges. Since most physical and chemical processes governing neuronal activity are temperature-dependent, naturally occurring fluctuations of brain temperatures may have important functional consequences, affecting various neural functions [11]. It has been also suggested that Focused microwave radiometry may provide the capability of also detecting electrical conductivity variations at microwave frequencies of excitable cell clusters, such as in the case of brain tissues under certain

psychophysiological conditions [12].

Taking into account the above considerations and findings, a prototype microwave radiometric system was designed, simulated, constructed and tested. The innovation of our system is the conformal L-notch microstrip patch antenna [17, 18] that is used as a single or in a two-element antenna array whereas a sensitive Dicke switch receiver operating at low microwave frequencies (1–3.5 GHz) completes the system. Its design and development has been based on detailed electromagnetic analysis while validation experiments have been performed using phantoms. Both temperature detection level and spatial resolution provided by the system have been estimated through this process.

2. THEORETICAL ANALYSIS

Microstrip circuits have been introduced to extend into the microwave range the benefits of printed circuit boards (PCB) widely employed at lower frequency. In specific applications like biomedical radiometry, microstrip patch antennas offer a considerable improvement in the radiator functional features: a) good heating efficiency in their boresight direction, b) small size, leading to better detectability (the smaller the antenna size, the smaller the malignancy that can be detected) and portability, c) ease of conformal and lightweight construction which improves coupling to body parts and d) ease of array combinations leading to extra detecting advantages [17]. The current utilization of microstrip antennas concerns the near-field electromagnetic (EM) energy detection from biological head tissue.

The simulation analysis of the relevant electromagnetic problem was numerically approached using the simulation software tool HFSS (Ansoft, Pittsburgh, PA) that implements the Finite Element Method (FEM). The human head modeling was accomplished both by a double layered hemisphere and the anatomically detailed two-layered SAM (Standard Anthropomorphic Mannequin) model [19] comprising in both cases two types of head tissues: brain matter, represented by the inner part, and skull, represented by the outer layer. In this analysis, two setups where examined each at two operating frequencies. The first setup involved the conformal L-notch microstrip patch antenna placed on the head models, while the second comprised a two element array of the same antenna type placed on the hemispheric head model only. Finally, in order to reduce the computational cost, the reciprocal electromagnetic problem is modeled and solved. According to the reciprocity theorem, a response of a system to a source is unchanged when source and measurer are interchanged. Hence, instead of placing

the source in the head model, the response of the head model to the excitation generated by an antenna positioned on its top, is calculated.

The antenna, was designed to exhibit a conformality of 20°, the feeding was done by a coaxial cable ending in an SMA connector with an inner diameter of 1.2 mm, and the substrate used was Rogers RO4350 with dielectric constant value $e_r = 3.66$. To overcome simple microstrip antennas' narrow bandwidth and single resonant frequency a special L cut was imported on the upper left corner of the rectangular microstrip patch antenna. This cut resulted to a multiband successful performance of the antenna (two resonant frequencies) and an enhancement of each frequency's bandwidth [17] a phenomenon that occurs as the notch introduces additional coupling between the upper edge of the rectangular patch and the ground plane [20]. Finally, it must be noted that the SMA position on the patch and the dimensions of the L-notch constitute influential parameters for matching the different impedances and defining the resonant frequencies and their bandwidth [21]. Conformality is also a key issue for the previous arrangements. In figure 1a the configuration and the optimal dimensions of the proposed antenna are presented while in Fig. 1(b) the first simulated setup with the conformal L-notch microstrip patch antenna placed on the hemispheric head model is shown.

The second setup was analyzed with a two element array of the conformal L-notch patch antenna at a respective top position on the
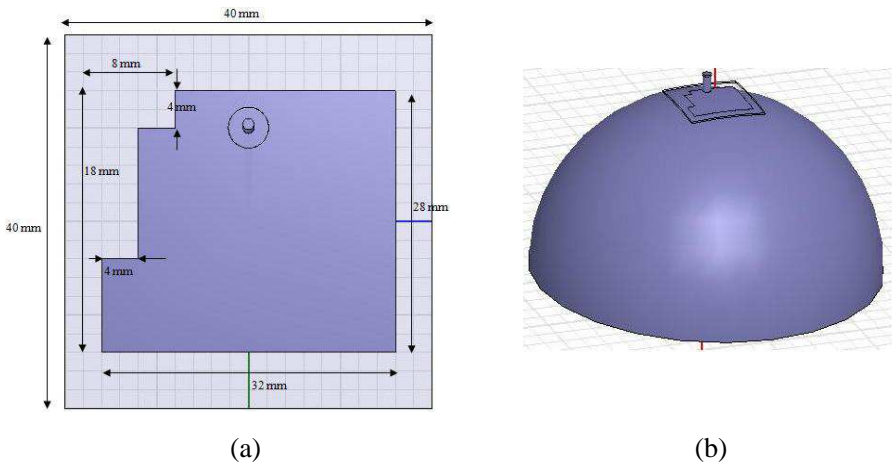

(a)   (b)

Figure 1. (a) The L-notch conformal patch antenna. (b) Conformal L-notch patch — hemisphere head model.

double layered hemisphere head model (respective configuration with Fig. 1(b). The SAM head model wasn't used in this case due to high computational cost.

2.1. Simulation Results

2.1.1. L-notch Antenna — Hemisphere Head Model

In the first simulated system (Fig. 1(b)), the values of the dielectric and conductivity characteristics of the head tissues (inner and outer model layer) were respective to the operating frequencies [22] and shown in Table 1. It is obvious from the numerical simulated results presented in this table that the antenna matched to the head model has two operating frequencies with satisfying reflection coefficients S_{11}.

Table 1. Numerical simulated results for L-notch antenna – double layered hemisphere system.

L-notch (single element)	Double layered hemisphere			
Operating frequency	2.44		2.6	
Relative permittivity	42.75 (brain)	15.1 (skull)	42.37 (br.)	14.86 (sk.)
Conductivity (S/m)	1.42 (brain)	0.56 (skull)	1.58 (br.)	0.63 (sk.)
S_{11}	−24.22 dB		−15.58 dB	
Bandwidth	53 MHz		45 MHz	
Detection depth	4.5 cm		4.1 cm	

In Fig. 2, the e-field distribution is depicted for the first resonant frequency of the system, with the second one exhibiting similar characteristics. As it can be observed, a single radiation lobe is originated from the center of the patch antenna, leading to a specific focused radiation region inside the head model. The detection depth is calculated from the e-field figures and is estimated 4.5 cm and 4.1 cm respectively for the two frequencies.

2.1.2. L-notch Antenna — SAM Head Model

Following, the double layered hemisphere was replaced by the SAM head model, with the respective constitutive parameters, and similar simulations were carried out with the system shown in Fig. 3 and numerical results presented in Table 2.

For the two operating frequencies of the system that are shown in Table 2, the *e*-field distribution is calculated. In Fig. 4(a), we have a view of the whole system in plane *Y*-*Z* at the first operating frequency (2.36 GHz), while in Fig. 4(b), we focus at the area of interest where the EM radiation is highly penetrating. Similar distribution results are obtained for the second operating frequency (2.74 GHz).

As with the simplest head model, a single radiation lobe is observed, originating from the center of the patch antenna and resulting in a specific focused radiation region inside the SAM model. The detection depth is estimated 4.2 cm and 4 cm respectively for the two frequencies.
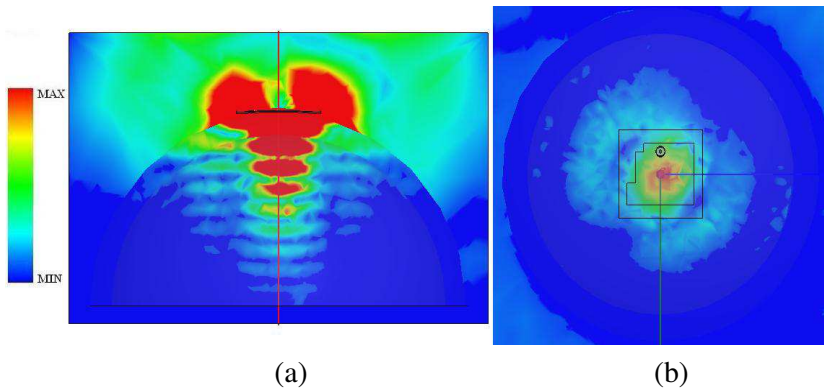

(a)   (b)

Figure 2. *E*-field distribution in conformal L-notch patch antenna — hemisphere model system, at 2.44 GHz: (a) *Y*-*Z* plane, (b) *X*-*Y* plane.
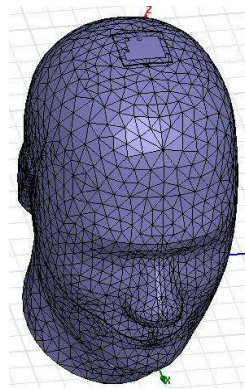

Figure 3. Conformal L-notch patch — SAM head model.

Table 2. Numerical simulated results for L-notch antenna — SAM head model system.

L-notch (single element)	SAM head model			
Operating frequency	2.36 GHz		2.74 GHz	
Relative permittivity	42.61 (br.)	15 (sk.)	42.19 (br.)	14.75 (sk.)
Conductivity (S/m)	1.48 (br.)	0.586 (sk.)	1.66 (br.)	0.67 (sk.)
S_{11}	-10 dB		-10 dB	
Bandwidth	~ 6 MHz		~ 6 MHz	
Detection depth	4.2 cm		4 cm	

Table 3. Numerical simulated results for two L-notch antennas (array) — double layered hemisphere system.

L-notch (two element array)	Double layered hemisphere			
Operating frequency	2.32		2.72	
Relative permittivity	42.75 (br.)	15.1 (sk.)	42.06 (br.)	14.67 (sk.)
Conductivity (S/m)	1.42 (br.)	0.56 (sk.)	1.73 (br.)	0.7 (sk.)
S_{11}	-12.23 dB	-15.09 dB	-14.67 dB	-20.79 dB
Bandwidth	16 MHz	33 MHz	65 MHz	58 MHz
Detection depth	4.2 cm		4 cm	

2.1.3. Two Element (L-notch Antenna) Array — Hemisphere Head Model

The simulations for the second examined system, as it can be observed in Table 3, gave again two well operating frequencies for the two element array adjusted to the hemisphere head model, with satisfying reflection coefficients S_{11} and enhanced bandwidth for both elements. In Fig. 5, the e-field distribution is depicted for the first operating frequency of the system (same for second frequency), with detection depth measured 4.2 cm and 4 cm respectively for the two frequencies.

2.1.4. L-notch Antenna(s) in Various Positions on Head Models

In order to enforce the value of the proposed system's simulation configurations and approach even more the practical system and its
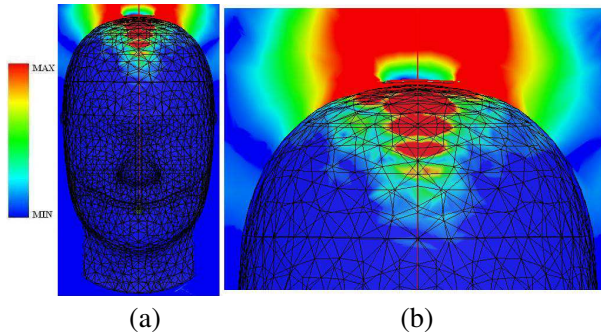
Figure 4. E-field distribution in conformal L-notch patch antenna — SAM head model system, at 2.36 GHz, plane Y-Z: (a) aspect of total system, (b) focus in area of interest.
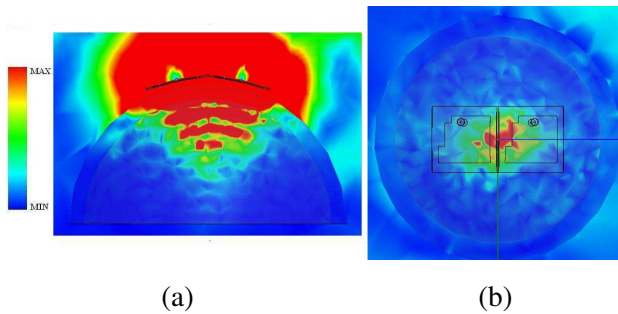

Figure 5. E-field distribution in two conformal L-notch patch antennas — hemisphere model system, at 2.32 GHz: (a) Y-Z plane, (b) X-Y plane.

respective experimental setups, simulations with the antenna(s) at various positions on the head models, indicating the source's respective different locations inside the head, were carried out. The results were proportional to the ones having the antenna(s) on the top of each head model whereas Fig. 6 depicts the e-field distribution for the first operating frequency of four indicative simulations; in Figs. 6(a)–(b) the conformal L-notch patch antenna(s) are located at the back of the hemisphere head model giving at 2.34 GHz (for both cases) a detection depth of 4.2 cm and 4.1 cm respectively, while in Figs. 6(c)–(d) the conformal L-notch patch antenna is located at the forehead and at the right hemisphere of the SAM model, giving at 2.32 GHz and 2.38 GHz respectively, a detection depth of 4 cm and 4.1 cm. The results are respective for the second, higher, operating antenna frequency of each simulation and for additional antenna positions tested.
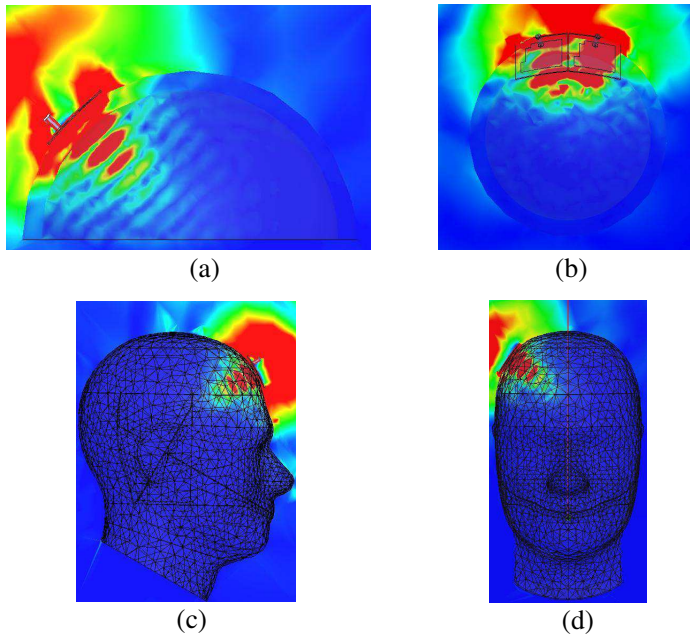
Figure 6. *E*-field distribution for: (a) one L-notch patch antenna at backside of hemisphere head model (*X*-*Z* plane), (b) two L-notch patch antennas at backside of hemisphere head model (*X*-*Y* plane), (c) L-notch patch antenna at forehead of SAM head model (*X*-*Z* plane), (d) L-notch patch antenna at right brain hemisphere of SAM head model (*Y*-*Z* plane).

## 3. EXPERIMENTAL PROCEDURE AND RESULTS

3.1. Methods

The constructed prototype passive microwave radiometry system (Fig. 7(a)) consists of a microwave receiver which comprises a sensitive radiometer and one or two (array) contact antennas (conformal microstrip patch antennas) that are used to receive the radiometric signals. Except this analogue part, a digital one also exists comprising a personal computer with the suitable equipment, in order to collect and process the data received from the experimental measurements.

The radiometer utilized was designed and constructed in our laboratory (Fig. 7(b)). It is a Dicke switch radiometer with operating ability in any frequency of the range 1–3.5 GHz, using a local oscillator. Each operating frequency has approximately 50 MHz bandwidth and an embedded internal LNA gives a 40 dB gain. The

Table 4. Measured parameters for conformal L-notch antenna (single and double element (array)) — experimental water phantoms systems.
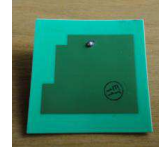
Conformal L-notch Antenna with Phantoms			
Number of antennas	Operating Frequency	S_{11}	Bandwidth
Single element	2.52 GHz	−17 dB	100 MHz
	2.83 GHz	−26.44 dB	105 MHz
Two elements (array)	2.53 GHz	−17.2 dB	108 MHz
	2.845 GHz	−18 dB	180 MHz
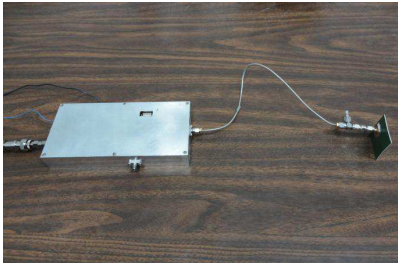
(a)
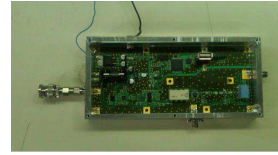
(b)

(c)

Figure 7. Passive microwave radiometry system.

radiometer's sensitivity ($\Delta T_{\min}$) is 0.02 K, whereas the whole system's sensitivity varies according to the antenna setup and will be recorded separately. Finally, the conformal L-notch patch antenna (Fig. 7(c)) was constructed exactly as designed in the previous section of this paper, and used as the system's receiving antenna. Its parameters (operating frequencies, S_{11}, bandwidth), presented in Table 4, were similar to the simulated ones (previous tables) and same for both experimental phantoms.

As already explained, the system's main goal is to serve as a brain intracranial device. Thus, some of its potential applications are temperature monitoring during hyperthermia sessions and functional brain imaging. These two different applications have one important similarity: specific regions inside the brain are of elevated temperature. As far as functional imaging is concerned, when a certain area of the brain is activated as a result of an external stimulus, the temperature in this area is slightly elevated from the "normal" level. Therefore, two experimental setups were tested. In the first one cylindrical
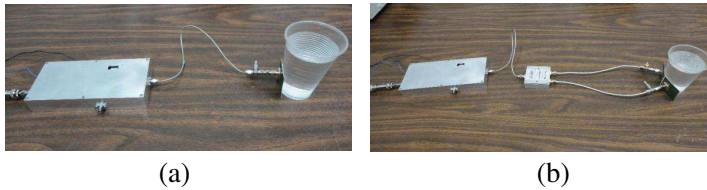
(a)   (b)

Figure 8. Experimental setups (one and two antennas), for temperature detection level.

phantom of the same size were used, containing deionized water at different temperatures, in order to determine the system's minimum temperature detection level. In the second one, a small container (filled with water at high temperature) models the cancerous tissue or the activated brain area, while the large container (filled with water at low temperature) models the surrounding healthy tissue or the inactivated region of the brain in order to investigate the system's capability to detect a warm area at a depth inside a cooler environment and examine its spatial sensitivity. All the experiments were performed in a Faraday-anechoic chamber.

3.2. Results

3.2.1. Temperature Detection Sensitivity

In the first experimental setup, two containers (named A) of the same size (radius 3 cm and height 9.5 cm) filled with deionized water, were used. The amount of water infused in them had a temperature difference depending on the detection level of each antenna setup, while the room temperature was 26°C. The sequence of this first procedure was as follows: from time $t = 0$ s until time $t = 50$ s, the system measured the background noise (baseline). Then, container A, filled with deionized water at a specific temperature, was placed in contact with the system's receiving antenna(s) until $t = 100$ s when it was removed. At $t = 150$ s a same container, with different water temperature, was placed again in contact with the antenna(s) until $t = 200$ s when it was also removed.

Figure 9 shows results of the radiometric output of the system at 2.52 GHz (1st operating frequency) for local temperature changes from 45°C to 42°C and 39°C to 36°C (meaning always the alternation of the containers with water of the temperatures in question). From the graphs, it can be clearly observed, the 3°C temperature difference for both regions under investigation (45°C–42°C and 39°C–36°C).
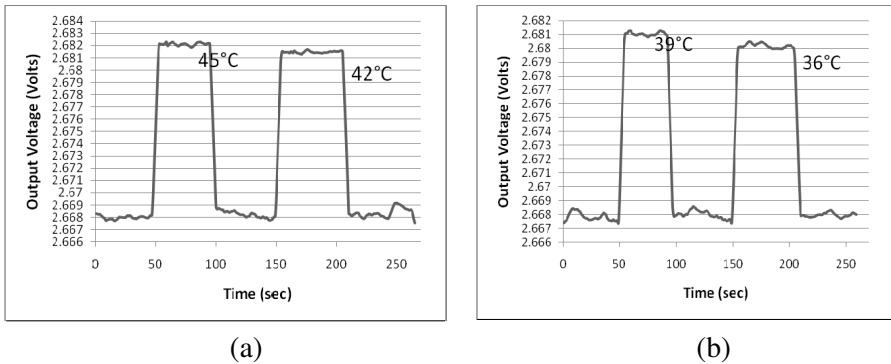
(a)   (b)

Figure 9. Radiometric output at $2.52\,\text{GHz}$ for detection of local temperature changes, using cylindrical phantoms: (a) 45°C–42°C, (b) 39°C–36°C.

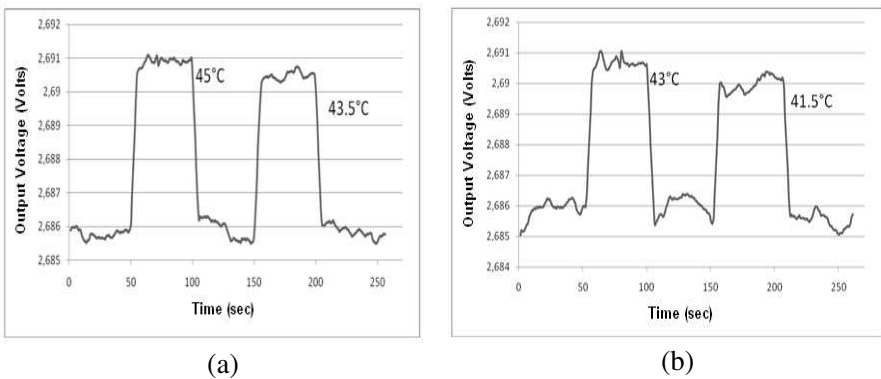(a)   (b)

Figure 10. Radiometric output at $2.53\,\text{GHz}$ (two element array antenna) for detection of local temperature changes, using cylindrical phantoms: (a) 45°C–43.5°C region, (b) 43°C–41.5°C region.

More specifically, the containers filled with water of 45°C and 39°C give a radiometric output $0.6\,\text{mV}$ greater than the ones of 42°C and 36°C respectively. Likewise, in the system's 2nd operating frequency ($2.83\,\text{GHz}$) the same temperature difference (3°C) is detected in the same temperature regions but exhibiting in this case a greater radiometric output of $1\,\text{mV}$. It is obvious, then, that with the specific antenna setup the examined device detects clearly the differences of the emitted radiation from the different phantoms showing a sensitivity of 3°C and a temperature precision of $0.2\,\text{mV/°C}$ and $0.333\,\text{mV/°C}$ for the 1st and 2nd operating frequency respectively.

Following exactly the same experimental procedure, an array of two conformal L-notch microstrip patch antennas (Fig. 8(b)) was used to receive the emitted radiometric signals. Due to better temperature sensitivity in this case, the temperature differences investigated were of the order of 1.5°C in the temperature range 45°C–35.5°C. In Fig. 10, we can see the graphs of the radiometric output voltage versus time for the first two cases at 2.53 GHz (1st operating frequency of the device). It is obvious that a 1.5°C temperature difference for both is detected, with the containers filled with water of 45°C and 43°C giving a radiometric output 0.5 mV greater than the ones of 43.5°C and 41.5°C, respectively. Relevant patterns with the same radiometric output voltage difference (0.5 mV) apply to all examined temperature regions in the aforementioned range for both operating frequencies (2.845 GHz is the 2nd, indicating that with the antenna array the examined device detects clearly the differences of the emitted radiation from the different temperature phantoms showing a sensitivity of 1.5°C and a temperature precision of 0.333 mV/°C for both resonant frequencies.

3.2.2. Detection Depth and Spatial Sensitivity

In the second experimental setup, a container B with radius 8 cm and height 5 cm and a sphere A with 5 cm diameter, both filled with deionized water, were used. It must be noted here that a percent measurement marking was made on the base of container B in order to be evident what the position of the sphere is at each measurement time. The sequence of this second procedure was as follows: Container B was filled with water of 37°C and placed in touch with the radiometric system's antenna(s) (Fig. 11). From time $t = 0$ s until $t = 60$ s, the system measured the background noise (baseline). Then, sphere A, filled with deionized water of 43°C, was placed inside container B until approximately $t = 110$ s when it was removed. Its positioning started from the contact location of container B with the receiving
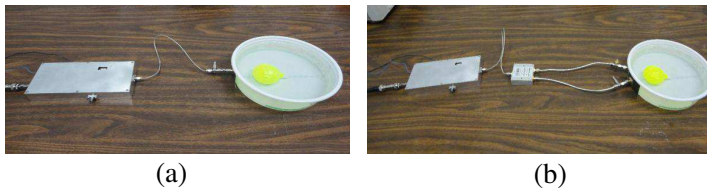

(a)   (b)

Figure 11. Experimental setups for detection depth and spatial sensitivity.

antenna(s) and moved along the measurement marking line. Sphere A occupies one and different position each time and all distances are measured from the point that the antenna(s) contact with container B (internally). Finally, it must be noted that primary test measurements showed for the single antenna setup that sphere A was detected only under its effective area and for the double array antenna setup that sphere A was detected under its center area, giving highly reduced radiometric voltage values at side positions of the sphere with regards to the array. Both results lead to the conclusion that the spatial sensitivity and directivity of the system is satisfying, localized inside the receiving antenna(s) main lobe area.

Figure 12 shows the results of the radiometric output of the single antenna system (Fig. 11(a)) at 2.52 GHz (1st operating frequency), for the first two of the five different positions that sphere A was placed inside container B. It is obvious that the sphere's position is detected in both cases and moreover, as it is placed away from the contact point of antenna(s) — container B, the difference of the measured radiometric voltage output, between the state that the sphere remains inside the container and the one of background noise (absence of object under measurement), is reduced. The previous are valid for all five measuring positions and both operating frequencies and are clearly presented in Table 5 where the voltage differences in relation to the position are shown. It is obvious that in the second operating frequency the detection depth is smaller than the first one.

Following exactly the same experimental procedure, an array of
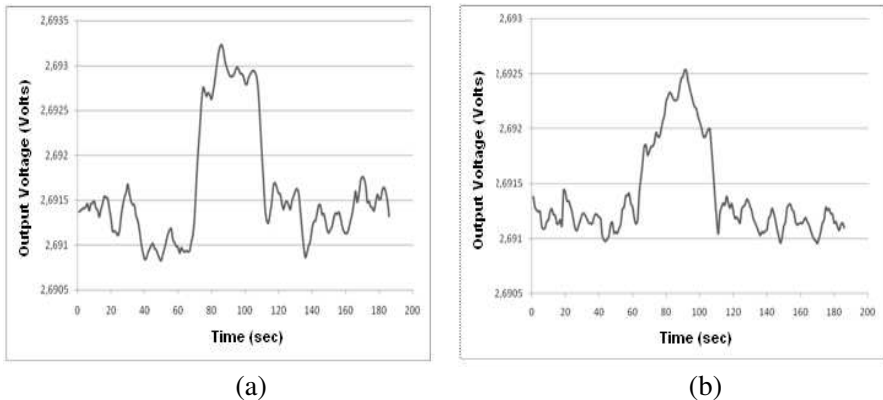

(a)   (b)

Figure 12. Radiometric output at 2.52 GHz (single antenna system) for detection of change in position of sphere A inside container B: (a) pos. 0 cm, (b) pos. 1 cm.

Table 5. Radiometric output difference with regard to sphere's A position inside container B (single antenna).

1st operating frequency 2.52 GHz		2nd operating frequency 2.83 GHz	
Position (cm)	Voltage difference (mV)	Position (cm)	Voltage difference (mV)
0	1.5	0	1.5
1	1	1	1.1
2	0.8	2	0.9
3	0.6	2.5	0.4
4	0.4		

Table 6. Radiometric output difference with regard to sphere's A position inside container B (two element array antenna).

1st operating frequency 2.53 GHz		2nd operating frequency 2.845 GHz	
Position (cm)	Voltage difference (mV)	Position (cm)	Voltage difference (mV)
0	0.8	0	0.6
1	0.5	1	0.5
2	0.4	2	0.4
3	0.3	2.5	0.3
3.5	0.2		

two conformal L-notch microstrip patch antennas (Fig. 11(b)) was used to receive the emitted radiometric signals. The results are of similar patterns like Fig. 12 and indicate clearly the detection of sphere's position in any case and the reduction of the measured radiometric voltage output as it is placed away from the contact point of antenna(s) — container B. In Table 6, the measurements are presented, indicating again that in the 2nd higher frequency the detection depth of the system is smaller than the 1st one.

4. CONCLUSION

In the past years, efforts have been made by our group to develop a passive, non-invasive system for brain intracranial applications. The present paper mainly aims at presenting a newly designed and developed multiband patch antenna for focused microwave radiometry monitoring. Numerical simulations using head models were carried out and verified in practice via proof-of-concept experimental phantom measurements.

The system discussed in this paper, has limitations concerning spatial accuracy and temperature resolution compared to other well-established technologies for imaging due to its entire passive character. Nevertheless, it is portable, entirely passive and seems promising to provide useful information regarding tissue temperature variations especially when used in conjunction with, or complementary to, other clinical tools. The brain, being the most complicated and important organ of our existence has structural characteristics and electromagnetic properties of high complexity. Thus, the proposed methodology needs continuous and rigorous investigation in order to reveal its potential value in clinical practice.

The theoretical electromagnetic simulated results lead to the conclusion that a portable contact radiometric imaging-diagnostic system could operate well with the conformal L-notch microstrip patch antenna as the receiving antenna array element. These findings were confirmed experimentally by constructing the actual device (microwave receiver, antennas and digital processing part) and performing the appropriate experiments inspired by its future clinical applications. The experimental measurements confirmed the ability of the device to detect either differences in temperature between small volumes of higher temperature or an area of higher temperature placed in a cooler environment.

All the previous results enforced the idea that the device in question could become potentially in the near future a clinical tool of temperature monitoring for diagnosis and during hyperthermia sessions. Future research will focus on designing and constructing new conformal microstrip patch antennas with special geometries, multiple feeds and metamaterial substrates [23–25] that will allow even smaller dimensions and multiband operating characteristics. Moreover, the use of antenna arrays with more elements and different configurations (e.g., phased arrays) constitute important parameters that may result in greater sensitivity and better directivity, with capability of dynamic focusing, to the system. For argument's sake, it is possible to create a single focusing point with sufficient detection depth using a phased array system comprising 4 patch antennas as shown in the past [26, 27]. In this paper, the aim is to study the new antenna as an element of the future array (initially the two antenna setup is tested herein) and at the same time the detection depth at several frequency bands is examined both theoretically and experimentally.

Finally, the participation of healthy volunteers in standard psychophysical tests constitutes also near future research aims.

REFERENCES

1. O'Halloran, M., M. Glavin, and E. Jones, "Rotating antenna microwave imaging system for breast cancer detection," *Progress In Electromagnetics Research*, Vol. 107, 203–217, 2010.

2. Zhou, H., T. Takenaka, J. Johnson, and T. Tanaka, "A breast imaging model using microwaves and a time domain three dimensional reconstruction method," *Progress In Electromagnetics Research*, Vol. 93, 57–70, 2009.

3. Conceicao, R. C., M. O'Halloran, M. Glavin, and E. Jones, "Comparison of planar and circular antenna configurations for breast cancer detection using microwave imaging," *Progress In Electromagnetics Research*, Vol. 99, 1–20, 2009.

4. Catapano, I., L. Di Donato, L. Crocco, O. M. Bucci, A. F. Morabito, T. Isernia, and R. Massa, "On quantitative microwave tomography of female breast," *Progress In Electromagnetics Research*, Vol. 97, 75–93, 2009.

5. Chen, G. P., W. B. Yu, Z. Q. Zhao, Z. P. Nie, and Q. H. Liu, "The prototype of microwave-induced thermo-acoustic tomography imaging by time reversal mirror," *Journal of Electromagnetic Waves and Applications*, Vol. 22, No. 11–12, 1565–1574, 2008.

6. Yu, J., M. Yuan, and Q. H. Liu, "A wideband half oval patch antenna for breast imaging," *Progress In Electromagnetics Research*, Vol. 98, 1–13, 2009.

7. Giamalaki, M. I., I. S. Karanasiou, and N. K. Uzunoglu, "Electromagnetic analysis of a non invasive microwave radiometry imaging system emphasizing on the focusing sensitivity optimization," *Progress In Electromagnetics Research*, Vol. 90, 385–407, 2009.

8. Hand, J., G. M. J. van Leeuwen, S. Mizushina, J. B. van de Kamer, K. Maruyama, T. Suiura, D. V. Azzopardi, and A. D. Edwards, "Monitoring of deep brain temperature in infants using multi frequency microwave radiometry and thermal modeling," *Phys. Med. Biol.*, Vol. 46, No. 6, 1885–1903, 2001.

9. Rosen, A., M. A. Stuchly, and A. V. Vorst, "Applications of RF/microwaves in medicine," *IEEE Trans. Microwave Theory Tech.*, Vol. 50, 963–974, 2002.

10. Dubois, L., J. P. Sozanski, V. Tessier, J. Camart, J. J. Favre, J. Pribetich, and M. Chivé, "Temperature control and thermal dosimetry by microwave radiometry in hyperthermia," *IEEE Trans. Microwave Theory Tech.*, Vol. 44, 1755–1761, 1996.

11. Karanasiou, I. S., A. Garetsos, K. T. Karathanasis, and N. K. Uzunoglu, "Development and laboratory testing of a non-

invasive intracranial focused hyperthermia system," *IEEE Trans. Microwave Theory Tech.*, Vol. 56, No. 9, 2160–2171, 2008.

12. Karanasiou, I. S., N. K. Uzunoglu, and C. Papageorgiou, "Towards functional non-invasive imaging of excitable tissues inside the human body using focused microwave radiometry," Special Issue on "Biological Effects and Medical Applications of RF/Microwaves" of the *IEEE Trans. Microwave Theory Tech.*, Vol. 52, No. 8, 1898–1908, Aug. 2004.

13. Corbett, R. J., A. Laptook, and P. Weatherall, "Noninvasive measurements of human brain temperature using volume-localized proton magnetic resonance spectroscopy," *J. Cereb. Blood Flow Metab.*, Vol. 17, 363–369, 1997.

14. Harris, B. A., P. J. D. Andrews, I. Marshall, T. M. Robinson, and G. D. Murray, "Forced convective head cooling device reduces human cross-sectional brain temperature measured by magnetic resonance: A non-randomized healthy volunteer pilot study," *Br. J. Anaesth.*, 100, 365–372, 2008.

15. Yablonskiy, D. A., J. H. Ackerman, and M. E. Raichle, "Coupling between changes in human brain temperature and oxidative metabolism during prolonged visual stimulation," *Proc. Nat. Acad. Sci.*, Vol. 97, 7603–7608, 2000.

16. Kiyatkin, E. A., "Physiological and pathological brain hyperthermia," *Prog. Brain Res.*, Vol. 162, 219–243, 2007.

17. Asimakis, N. P., I. S. Karanasiou, and N. K. Uzunoglu, "Conformal L-notch patch antennas for human brain monitoring using the SAM head model," *International Conference on Electromagnetics in Advanced Applications, ICEAA'09*, 214–217, Sep. 14–18, 2009.

18. Chen, Y.-P., H.-J. Sun, and X. Lv, "Novel design of dual-polarization broad-band and dual-band printed L-shaped probe-fed microstrip patch antennas," *Journal of Electromagnetic Waves and Applications*, Vol. 23, No. 2–3, 297–308, 2009.

19. Wu, B., "Comparative study of numerically computed spatial peak SAR values in uniformly scaled sam head models exposed to mobile phone radiation," *International Symposium on Electromagnetic Compatibility, EMC 2007*, Oct. 23–26, 2007.

20. Jung, J., W. Choi, and J. Choi, "A compact broadband antenna with an *L*-shaped notch," *IEICE Transaction on Communication*, Vol. E89-E, No. 6, 1968–1971, Jun. 2006.

21. Kumar, G. and K. P. Ray, *Broadband Microstrip Antennas*, Chapter 1, Artech House, USA, Boston, 2003.

22. Gabriel, S., R. W. Lau, and C. Gabriel, "The dielectric properties of biological tissues: II. Measurements in the frequency range 10 Hz to 20 GHz," *Phys. Med. Biol.*, Vol. 41, 2251–2269, 1996.

23. Lee, J. N. and J. K. Park, "Design of multi-band antenna with F-shaped slot," *Journal of Electromagnetic Waves and Applications*, Vol. 24, No. 2–3, 179–188, 2010.

24. Lin, C., F.-S. Zhang, Y. Zhu, and F. Zhang, "A novel three-fed microstrip antenna for circular polarization application," *Journal of Electromagnetic Waves and Applications*, Vol. 24, No. 11–12, 1511–1520, 2010.

25. Shi, S. J., L. H. Weng, Y. Y. Yang, X. Q. Chen, and X. W. Shi, "Design of wideband dissymmetric E-shaped microstrip patch antenna," *Journal of Electromagnetic Waves and Applications*, Vol. 23, No. 5–6, 645–654, 2009.

26. Oikonomou, I., S. Karanasiou, and N. K. Uzunoglu, "Phased-array near field radiometry for brain intracranial applications," *Progress In Electromagnetics Research*, Vol. 109, 345–360, 2010.

27. Oikonomou, I., S. Karanasiou, and N. K. Uzunoglu, "Potential brain imaging using near field radiometry," *Journal of Instrumentation*, JINST 4 P05017, 2009.